



 Cite this: *RSC Adv.*, 2024, 14, 33007

# Optical detection of uric acid based on a citric acid functionalized copper-doped biochar nanozyme

 Noaman Khan,<sup>a</sup> Mansoor Ahmad,<sup>b</sup> Wei Sun,<sup>b</sup> Noor S. Shah,<sup>c</sup> Muhammad Asad,<sup>a</sup> Mohibullah Shah,<sup>d</sup> Riaz Ullah,<sup>e</sup> Mohamed A. Ibrahim,<sup>f</sup> Amir Badshah<sup>\*a</sup> and Umar Nishan  <sup>\*a</sup>

Uric acid is the end product of purine metabolism and is a key biomarker for various diseases. Under normal conditions, there is a balance between its production and excretion. Its higher concentration can cause inflammation and severe pain, which makes it necessary to monitor its level for the diagnosis, management, and treatment of various pathological conditions. The current work reports on the synthesis of a copper-doped biochar (Cu@BC) nanocomposite and its functionalization with citric acid. The synthesis of the mimic enzyme was confirmed through various spectroscopic techniques. The nanozyme catalyzes hydrogen peroxide to oxidize tetramethylbenzidine (TMB) with an optical change from colorless to blue-green. This optical transformation was confirmed through a UV-vis spectrophotometer, which gave an expected  $\lambda_{\text{max}}$  of 652 nm characteristic of TMB<sub>oxi</sub>. The incorporation of uric acid into this reaction mixture resulted in the reduction of TMB<sub>oxi</sub> to TMB<sub>red</sub>, accompanied by an optical change from blue-green to colorless, which was again confirmed with a UV-vis spectrophotometer. The fabricated sensor's performance was finely-tuned to report on its various key components. The best response was achieved at 2 mg of the nanozyme, pH 6, time 150 seconds, TMB, and hydrogen peroxide 0.9 and 1.5 mM, respectively. Under the above-mentioned optimized conditions, the fabricated sensor detected uric acid in the range of 1–90  $\mu\text{M}$  with limits of detection and quantification of 0.17 and 0.58  $\mu\text{M}$ , respectively, with an  $R^2$  of 0.997. The proposed sensor was highly selective and successfully detected uric acid in real sample solutions.

 Received 17th August 2024  
 Accepted 14th October 2024

DOI: 10.1039/d4ra05976j

[rsc.li/rsc-advances](https://rsc.li/rsc-advances)

## 1 Introduction

Uric acid is the final product produced from the metabolism of purine in the human body.<sup>1</sup> The permissible range of uric acid is 120–520  $\mu\text{M}$  in human serum and 1.4–4.4 mM in urine. In normal human physiology, there is a balance between its production and excretion. However, diet patterns and several other factors can result in a rise in the generation of uric acid. A steady increase in the level of uric acid has been observed in several people due to a change in diet pattern.<sup>2,3</sup> The excess formation of uric acid results in the formation of monosodium

urate crystals, which can be deposited in the joints. This can cause inflammation and severe pain. This abnormal level of uric acid is closely related to various diseases like Lesch–Nyhan syndrome, gout, hyperuricemia, renal failure, *etc.*<sup>4,5</sup> Therefore, accurate monitoring of the level of uric acid in human blood and urine can help in the diagnosis and management of various diseases.

Numerous analytical strategies, namely, fluorescence,<sup>6</sup> chromatography,<sup>7</sup> electrochemistry,<sup>8</sup> capillary electrophoresis,<sup>9</sup> uricase-based systems, *etc.*,<sup>10</sup> have been reported for the accurate determination of uric acid in blood or urine. The mentioned methods have achieved good results, but still they have numerous shortcomings. These include high cost, the need for skilled personnel, sample pretreatment steps, and time consumption, to name a few. Conversely, the colorimetric method offers an alternative with greater flexibility, viability, accuracy, simplicity, and easy operation.<sup>11</sup> Colorimetric methods can employ natural enzymes such as horse reddish peroxidase and alkaline phosphatase.<sup>12,13</sup> However, the problems associated with the natural enzymes, such as their high cost, difficult maintenance, narrow range-bound temperature, and pH requirements, limit their viability.<sup>14</sup> The rise of mimic enzymes has resulted in a great interest in the fabrication of

<sup>a</sup>Department of Chemistry, Kohat University of Science and Technology, Kohat 26000, KP, Pakistan. E-mail: [amirqau@yahoo.com](mailto:amirqau@yahoo.com); [umarnishan85@gmail.com](mailto:umarnishan85@gmail.com)

<sup>b</sup>Hainan International Joint Research Center of Marine Advanced Photoelectric Functional Materials, College of Chemistry and Chemical Engineering, Hainan Normal University, Haikou 571158, P. R. China

<sup>c</sup>Department of Chemistry, COMSATS University Islamabad, Abbottabad Campus, 22060, Pakistan

<sup>d</sup>Department of Biochemistry, Bahauddin Zakariya University, Multan 66000, Pakistan

<sup>e</sup>Department of Pharmacognosy, College of Pharmacy, King Saud University, Riyadh, Kingdom of Saudi Arabia

<sup>f</sup>Department of Pharmaceutics, College of Pharmacy, King Saud University, Riyadh 11451, Saudi Arabia



colorimetric biosensors. In mimic enzymes, nanobiosensors have become a central point of attention for the research community. In addition, colorimetric sensors offer the advantage of naked-eye detection of the progress of a reaction.<sup>15,16</sup>

Despite their easy synthesis, tunable properties, and high catalytic activity, the evolution of nanomaterials has been held back by their tendency to agglomerate. This agglomeration of the nanomaterials causes polydispersity and a reduction in surface area, which results in a decrease in their catalytic activity.<sup>17,18</sup> For this purpose, it is of utmost importance to achieve a homogenous distribution of nanomaterials to realize their true potential. The best strategy to overcome the agglomeration of nanomaterials is to use them in the form of composites. Different matrix materials have been used to keep the nanomaterials in homogeneous, dispersed form in the composite.<sup>15,19,20</sup>

Biochar is a commonly used matrix material that is produced through the pyrolysis of various feedstocks, ranging from agricultural residues to organic waste materials.<sup>21</sup> Biochar has a wide surface area, a nanoporous structure, high reactive functionalities, a high level of conductivity, low cost, is biocompatible, and is ubiquitous.<sup>22</sup> In addition, the renewable nature of the raw materials for its production makes it a favorable choice as a deagglomerating agent.<sup>23</sup> Owing to the carbonaceous nature of biochar, its metal-based nanocomposites can easily be recycled.<sup>24</sup> In addition, the nanocomposite was further macerated with citric acid to enhance its deagglomeration, biocompatibility, and conductivity. The selected capping and deagglomeration agent, *i.e.*, citric acid, causes thermodynamic stability and is widely used as a coating material. It changes the surface charge and leaves additional carboxyl groups on the surface of nanoparticles.<sup>25</sup>

Transition metal-based nanoparticles have been a common focus of attention in recent years. Various metal- and metal oxide-based nanoparticles have been used so far. Among them, copper is an element that functions as a coenzyme in the body, is involved in various biological functions, and has lower toxicity.<sup>26</sup> Copper-based nanomaterials have been used for the diagnosis of several biomarkers.<sup>27</sup> Owing to their impressive properties, copper nanoparticles were impregnated on the surface of biochar and further functionalized with citric acid.

The novelty of this work lies in the fabrication and use of citric acid-functionalized copper biochar (CA-Cu@BC), a mimic enzyme for the colorimetric sensing of uric acid. The synthesis of the proposed mimic enzyme (CA-Cu@BC) was confirmed by the use of various techniques. In this way, a new, fast, sensitive, and selective method was developed for the sensing of uric acid. The progress of the proposed sensor was monitored through the use of the chromogenic substrate TMB (3,3',5,5'-tetramethylbenzidine). Optimization experiments were performed to find the best performance of the fabricated mimic enzyme for the quantitative sensing of uric acid. The developed sensor with optimized conditions was successfully used to quantitatively assess uric acid in physiological solutions.

## 2 Experimental

### 2.1 Reagents and materials

Analytical-grade chemicals were used in all the experiments. All the chemicals were used as received without any further purification. Uric acid, TMB, CuSO<sub>4</sub>·5H<sub>2</sub>O, and sodium borohydride were acquired from Sigma-Aldrich. Other chemicals, such as citric acid and DMSO, were purchased from Daejung, South Korea. For the preparation of solutions, fresh double-distilled water, distilled in our lab, was used.

### 2.2 Instrumentation

Fourier transform infrared spectroscopy analysis for the prepared material was performed using a thermonicolet Waltham, MA, 5700 spectrometer. The analysis was performed in the range of 4000–400 cm<sup>-1</sup>. For sample preparation, a few mg of the sample was mixed with KBr, and its pellets were formed *via* pressing. A UV-vis spectrophotometer acquired from Shimadzu, Japan, model no. 1800, was used throughout the experimental process for scanning the absorption spectra. For this purpose, quartz cuvettes were used and filled about 2/3 with the prepared sample solution. A ZEISS Gemini 500 Germany scanning electron microscope coupled to an EDS was used to study the surface morphology and elemental composition of the synthesized material, respectively. A JEM-2100F microscope (JEOL, Japan) transmission electron microscope was employed to study the microstructure of the prepared nanocomposite. The samples were dispersed evenly on double-sided conductive carbon tape attached to the SEM stub. The phase and crystallite size of the synthesized material were studied through a Bruker AXS D8 X-ray diffractometer. The samples were evenly distributed on flat surfaces and placed in an XRD holder. X-ray photoelectron microscopy was performed to report on the chemical environment of each element on the surface of the synthesized material using Escalab 250Xi (Thermo, USA). The samples were placed on indium foil, and the powder was pressed for even distribution. A biochar kiln with controllable temperature was used for the preparation of biochar from date palm roots. The thermal stability of the synthesized Cu@BC was assessed through Pyris-1, V-3.81 PerkinElmer. The heating rate was maintained at 10 °C min<sup>-1</sup> from temperature to 800 °C under a nitrogen environment. The obtained data from these techniques was analyzed using standard protocols for the mentioned techniques.

### 2.3 Preparation of biochar

The biochar was prepared using the biomass obtained from date palm (*Phoenix dactylifera*) root. The root was washed several times with water to remove dirt and other adhering materials. After washing, the biomass was dried and then pyrolyzed in a biochar kiln at 450 °C for 80 minutes, according to the earlier reported protocol.<sup>28</sup> After the completion of the reaction, the reaction assembly was allowed to cool to room temperature. The biochar thus produced was taken out of the kiln and stored in plastic bottles for further use.

## 2.4 Preparation of the composite

The preparation of the copper-doped biochar (Cu@BC) nanocomposite was performed in an airtight flask under the continuous supply of nitrogen gas. For this purpose, (A) 1 gram of biochar was suspended in 50 mL of water/ethanol (9 : 1), followed by the addition of 50 mL of water solution containing 2.5 gram of  $\text{CuSO}_4 \cdot 5\text{H}_2\text{O}$ . (B) On the other hand, 2.5 g of  $\text{NaBH}_4$  was dissolved in 70 mL of water. Solution (B) was added dropwise into solution (A) with continuous stirring for 6 hours. The solution mixture was centrifuged, and the supernatant was removed. The solid precipitate was washed with ethanol and kept in an oven for 20 hours at 60 °C for drying.<sup>29</sup> The percentage yield was calculated to be 52%.

## 2.5 Functionalization of the material

To further enhance conductivity and deagglomeration, the synthesized materials were functionalized with citric acid. For this purpose, 0.5 g of citric acid was dissolved in 6 mL of ethanol and stirred for 30 minutes. Subsequently, 1 g of Cu@BC was added to it and stirred again for 60 minutes. Afterwards, the solution mixture was dried at room temperature to obtain CA-Cu@BC nanocomposites. The as-prepared material was kept in an airtight bottle for further use.

## 2.6 Colorimetric sensing of uric acid

For the colorimetric sensing of uric acid, various constituents of the proposed sensor were reacted together in an Eppendorf tube. For this purpose, 2 mg of the nanozyme, 250  $\mu\text{L}$  of PBS solution (pH 6), 100  $\mu\text{L}$  of TMB (0.9 mM), and 100  $\mu\text{L}$  of  $\text{H}_2\text{O}_2$  (1.5 mM) were added together. This resulted in an optical change that was visible to the naked eye and also confirmed through a UV-vis spectrophotometer. This was followed by the addition of the analyte (uric acid) at a specific concentration and incubation for a specific time. At ambient temperature, the reaction was monitored to detect optical changes in the solution mixture. The absorption spectra of the final solution were recorded using a UV-vis spectrophotometer. Finally, the fabricated sensor was successfully applied for sensing uric acid in real samples. The work was approved by the ethical committee of Kohat University of Science and Technology, *via* No. KUST/Ethical Committee/1628.

# 3 Results and discussion

## 3.1 Characterization results

Before the application of the synthesized mimic enzyme, its synthesis was confirmed with the help of the following techniques.

**3.1.1 FTIR and thermal analysis.** The functional group analysis of the fabricated mimic enzyme was performed through FTIR analysis, as shown in Fig. 1(A). The spectrum revealed a broad band in the range of 3550–3100  $\text{cm}^{-1}$  indicating the presence of a hydroxyl group involved in hydrogen bonding. The presence of this broad band can be attributed to the presence of moisture adsorbed from the air. A short peak around 2920  $\text{cm}^{-1}$  can be assigned to the C–H stretching

vibration of the alkyl moiety present in the nanozyme. A band around 2250  $\text{cm}^{-1}$  can be attributed to the presence of absorbed  $\text{O}=\text{C}=\text{C}$  in the fabricated material. The peaks around 1580, 1350, and 1120  $\text{cm}^{-1}$  indicate the presence of C=C, O–H (bending), and C–O–C respectively. A peak around 650  $\text{cm}^{-1}$  indicates the presence of doped copper in biochar.

To assess the thermal stability of the synthesized Cu@BC composite, thermal gravimetric analysis was carried out as shown in Fig. 1(B). The first prominent weight loss occurs at around 100 °C and can be attributed to the loss of moisture from the synthesized nanocomposite. A further increase in temperature leads to steady weight loss, which could be attributed to the various organic moieties in the biochar. At around 500 °C, the loss in weight almost becomes constant, and the char yield is around 65% at 750 °C. These results suggest the high thermal stability of the synthesized nanocomposite.

**3.1.2 XRD analysis.** The XRD diffractogram of the synthesized material can be seen in Fig. 1(C). It indicates that the doping of copper in biochar was successful based on the peaks that corresponded to  $\text{Cu}_2\text{O}$ . The reflections in the 2 theta range of 21–80 are in line with the  $\text{Cu}_2\text{O}$  polycrystalline phase. The presence of sharp peaks confirms the crystalline nature of the fabricated material. The peaks at  $2\theta$  values of 29.6, 36.46, 42.33, 61.33, 73.45, and 77.21° correspond to the cuprous oxide and could be attributed to its planes (110), (111), (200), (220), (220), and (222) planes, respectively, matched well with ICDD #01–078–2076.<sup>30</sup> Along with  $\text{Cu}_2\text{O}$ , there are two other forms of copper, *i.e.*, zero-valent copper and CuO, as indicated in the XPS study. However, they are not shown in the XRD diffractogram, which might be due to the smaller amount.

**3.1.3 Morphological studies.** SEM analysis was carried out to study the structural morphology of the synthesized material, as shown in Fig. 1(D). From the SEM image, it is clear that the surface of the prepared material is rough. Spherical particles were uniformly distributed on the surface of biochar without any agglomeration. This uniform distribution is highly essential for the catalytic role of the synthesized material. In the inset histogram, particle size distribution was calculated using SEM images of the synthesized material by ImageJ software. The average particle size was calculated to be 39.158 nm. Energy dispersive X-ray analysis was used to study the elemental composition of the synthesized material Cu@BC, as shown in Fig. 1(E) and inset table. The results show the successful incorporation of copper into the biochar. The microstructure of the synthesized nanocomposite was studied through transmission electron microscopy, as shown in Fig. 1(F and G). It is clear from the images that the Cu-based nanoparticles are deposited homogeneously on the surface of the transparent layered structure of biochar. A further insight was obtained through high-resolution transmission electron microscopy (HRTEM), as can be seen in Fig. 1(H). The lattice fringes in the image clearly indicate the crystalline nature of the deposited nanoparticles on the surface of biochar, corroborating the findings of XRD. To further confirm the distribution of various elements in the synthesized material, elemental mapping was performed. The results suggest the presence of carbon, oxygen, and copper in the synthesized nanocomposite. In addition, all



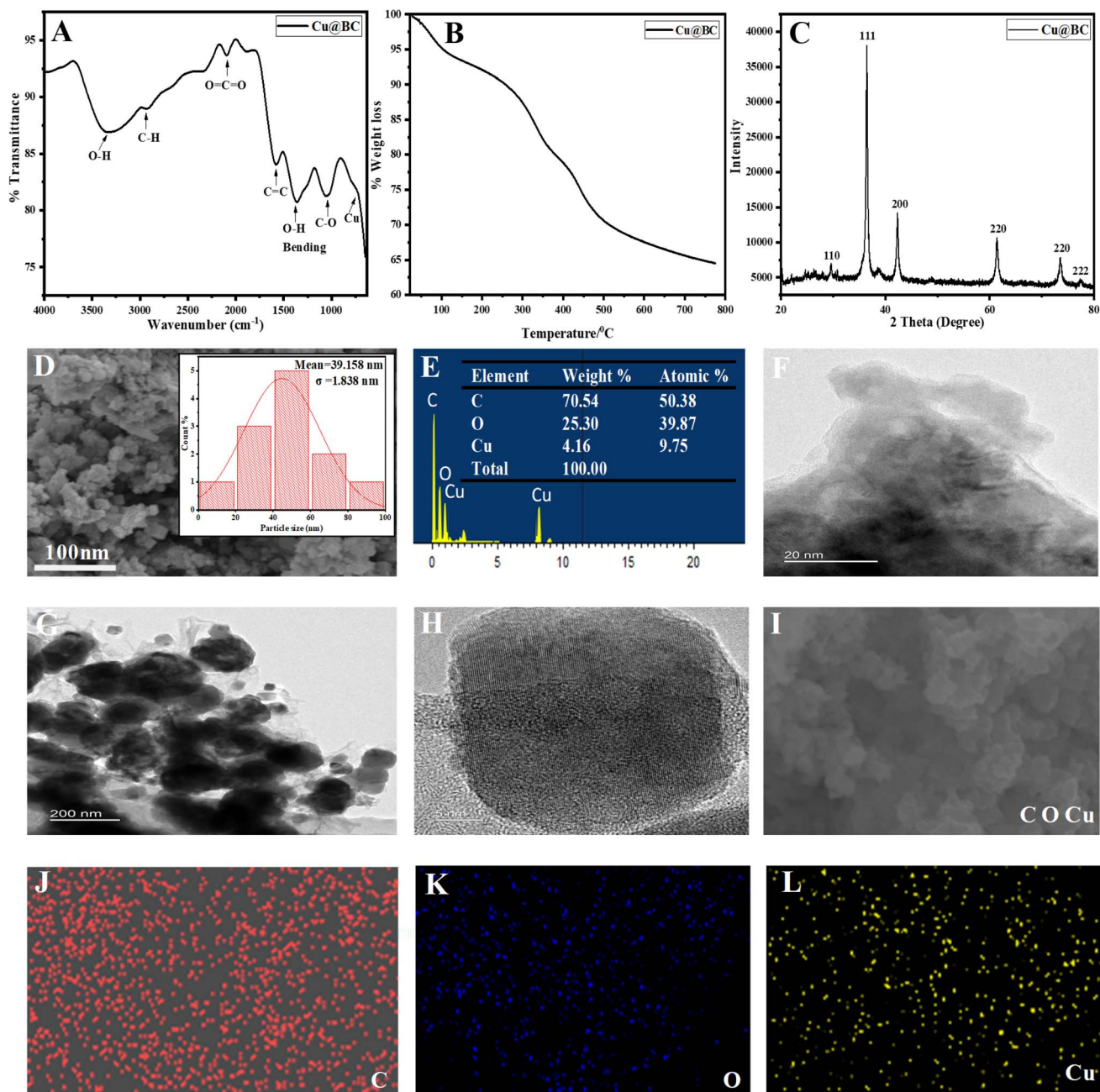


**Fig. 1** (A) FTIR analysis of the prepared Cu@BC showing the characteristic peaks of biochar as well as the characteristic peak of doped Cu–O. (B) Thermal gravimetric analysis showing the high thermal stability of the synthesized material up to 800 °C. (C) The XRD spectrum of the synthesized Cu@BC has sharp peaks indicating the crystalline nature of the fabricated material. (D) SEM analysis of the synthesized Cu@BC shows a rough surface morphology and a uniform distribution of spherical-shaped Cu nanoparticles. (E) EDX analysis of the prepared material showing the successful doping of Cu on the biochar matrix material. The inset table shows the elemental composition in terms of weight and atomic percentage of the synthesized material. (F and G) are the TEM images indicating the deposition of copper nanoparticles on the surface of biochar. (H) In the HRTEM image, the presence of lattice fringes indicates the crystalline nature of the copper nanoparticles. The images (I–L) demonstrate the elemental mapping of the synthesized material with the presence of the constituent elements present with uniform distribution necessary for their catalytic activity.

these elements are homogeneously and uniformly grown on the surface of matrix material, as depicted in Fig. 1(I–L).

**3.1.4 XPS analysis of the synthesized material.** Through X-ray photoelectron spectroscopy (XPS) analysis, the surface chemical state of the elements present in the synthesized material was studied, as shown in Fig. 2. The survey spectrum

shown in Fig. 2(A) reports the presence of constituent elements on the surface of the synthesized material. The major peak in the range of 925–960 eV can be attributed to Cu 2p. Similarly, the O 1s was found to be in the range of 526–536 eV. In addition, C 1s showed binding energy values in the range of 280–292 eV. Further deconvolution of the spectrum of Cu 2p (spectrum B)

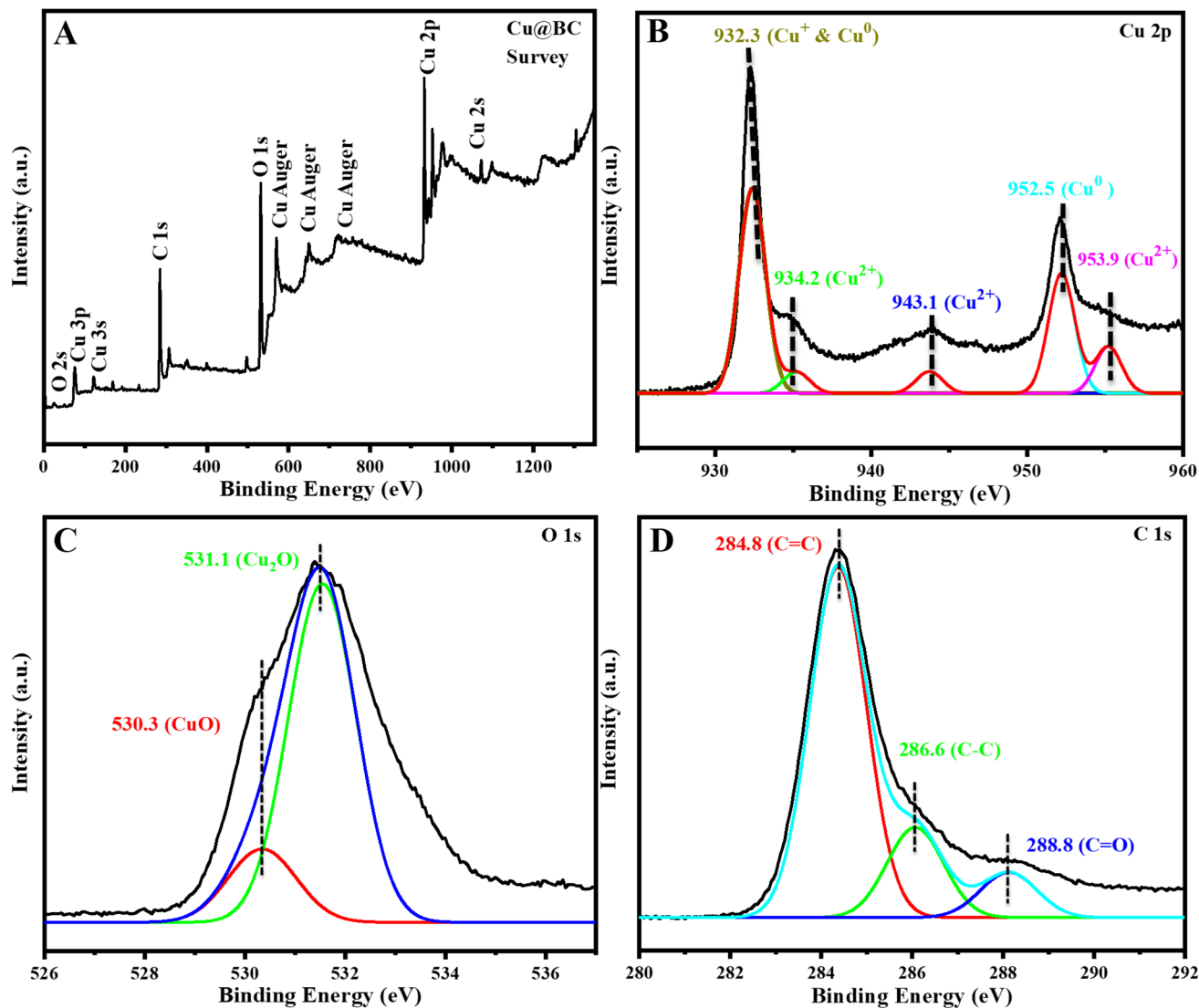


Fig. 2 (A) shows the survey spectrum indicating the presence of Cu 2p, O 1s, C 1s, and Cu Auger peaks at their corresponding positions in the synthesized material. (B) Shows the presence of  $\text{Cu}_2\text{O}$ , Cu, and residual CuO at their respective binding energies in the deconvoluted spectrum of Cu 2p. (C) Depicts the presence of oxygen at its respective binding energies in CuO and  $\text{Cu}_2\text{O}$  form. (D) Represents the presence of C=C, C–C, and C=O at their respective binding energies.

centered at 932.2 eV indicates the presence of  $\text{Cu}_2\text{O}$ . The peaks centered at 932.2 and 952.5 eV show the presence of zerovalent copper. Furthermore, the peaks centered at 934.2, 943.1, and 953.9 eV correspond to the residual CuO present in the synthesized nanocomposite.<sup>31,32</sup> In the case of Fig. 2(C), the representative XPS spectrum for O 1s with two peaks centering at 530.3 and 531.1 indicates the presence of CuO and  $\text{Cu}_2\text{O}$ . Fig. 2(D) represents the deconvoluted spectrum of C 1s with three peaks centering at 284.8, 286.6, and 288.8 indicating the existence of carbon in the form of C=C, C–C, and C=O, respectively.

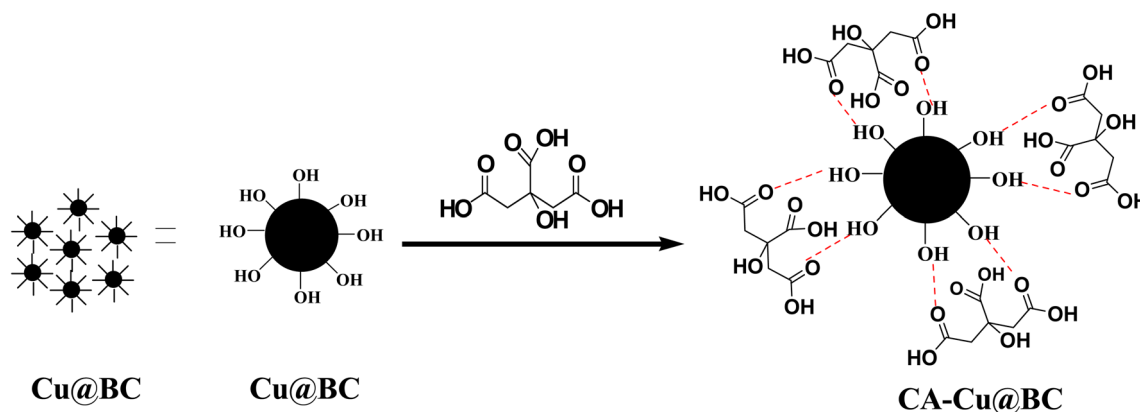
### 3.2 Functionalization of the synthesized material

After the confirmation of the synthesis of Cu@BC by various techniques, the synthesized material was functionalized by citric acid. The selection of citric acid as a functionalization

agent was preferred owing to its biocompatible nature, abundant availability, and low cost. This deagglomeration agent coated on the surface of the material (Cu@BC) produces a negative charge over the surface. These charges repel each other and keep the particles away from each other, so the surface area needed for catalytic reactions remains intact. In addition, it further increases the electron density and enhances conductivity on the synthesized platform. The schematic representation of the functionalization of Cu@BC to CA-Cu@BC is shown in Scheme 1.

### 3.3 Proof of concept experiment

In an effort to prove the efficacy of the synthesized mimic enzyme, the reaction of chromogenic substrate oxidation was performed in the presence and absence of the nanozyme. It is clear from Fig. 3 that, in the absence of the mimic enzyme,



Scheme 1 Schematic representation of the deagglomeration and surface functionalization achieved through capping of Cu@BC with citric acid.

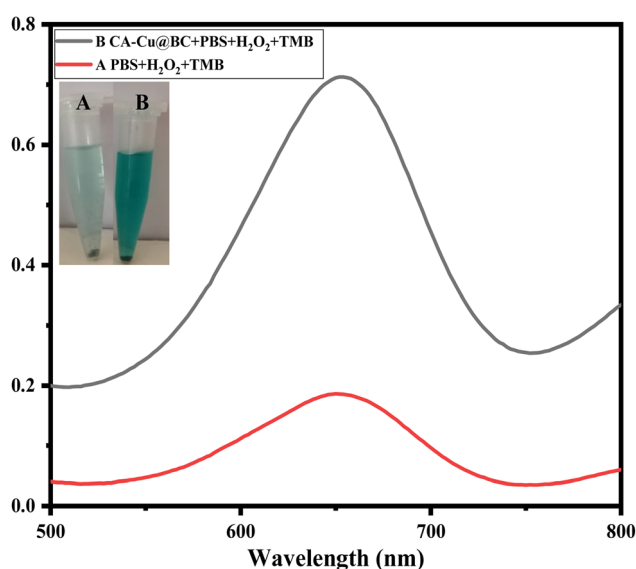


Fig. 3 Both (A and B) and their corresponding spectra show the role of the synthesized mimic enzyme (CA-Cu@BC) in the oxidation of the chromogenic substrate TMB under the prevailing conditions.

hydrogen peroxide was able to oxidize TMB to a minimal extent under the prevailing conditions. The UV-vis spectrum of the reaction showed a less intense peak due to the lower amount of oxidized TMB. On the other hand, in the presence of the mimic enzyme, the oxidation of TMB resulted in an intense peak and color of TMB, as shown in the figure. It indicates that the fabricated mimic enzyme catalyzes the oxidation of TMB effectively.

### 3.4 Optical detection of uric acid

Hydrogen peroxide, with the assistance of the proposed mimic enzyme (CA-Cu@BC), transforms the chromogenic substrate (TMB) into its oxidized form. This oxidation of TMB was visualized by the appearance of a blue-green color, and confirmation was done through a UV-vis spectrophotometer. This reaction set the stage for the incorporation of the analyte (uric acid) into the reaction mixture. The addition of uric acid results

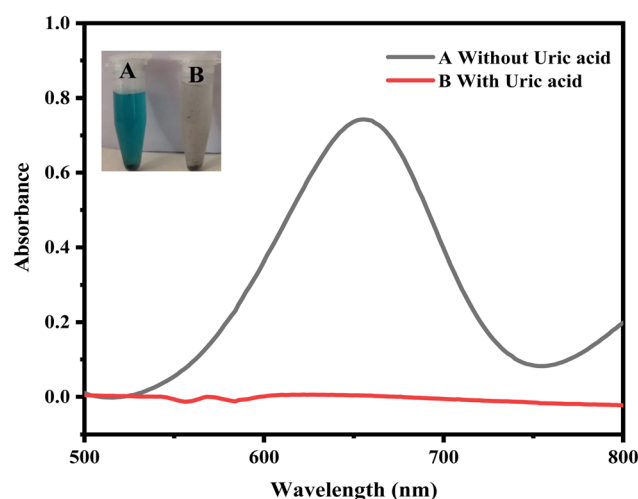
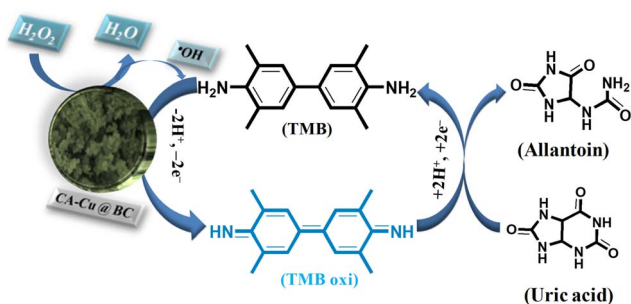


Fig. 4 UV-vis spectra and corresponding optical changes before (A) and after (B) the addition of the uric acid. The addition of uric acid diminishes the peak of TMB, resulting in its reduction.

in a visible optical transformation from blue-green to colorless. This can be explained by the reduction of TMB accompanied by the oxidation of uric acid. This reduction was visualized through the unaided eye and confirmed again through a UV-vis spectrophotometer. The adjoining Fig. 4 shows the UV-vis spectra and the optical change visible to the naked eye during the course of the reaction.

### 3.5 Proposed mechanism of the reaction

Hydrogen peroxide, with the catalytic assistance of a fabricated mimic enzyme (CA-Cu@BC), catalyzes the oxidation of TMB. This oxidation is triggered by the production of hydroxyl free radicals generated by the homolytic splitting of hydrogen peroxide. This generation of hydroxyl free radicals and the hemolytic splitting of hydrogen peroxide are not enough to adequately oxidize TMB. Here, the role of the mimic enzyme becomes crucial. Due to the enrichment of electron density, the mimic enzyme expedites the generation of abundant hydroxyl free radicals. These increased numbers of hydroxyl-free radicals



**Scheme 2** Mechanistic representation of the sensing of uric acid through hydrogen peroxide with the catalytic assistance of the mimic enzyme (CA-Cu@BC). TMB acts as a chromogenic substrate and visually assists in monitoring the progress of the reaction.

attack the chromogenic substrate (TMB). As a result of this, extensive oxidation of TMB takes place, and the color of the solution mixture changes from colorless to an intense blue-green color.

Mechanistically, this oxidation results in the conversion of the benzoid form of TMB into the quinoid form. This results in an increase in conjugation, and the energy gap between the frontier orbitals decreases. As a result of this, a red shift occurs, and the absorption takes place in the visible region at  $\lambda_{\text{max}}$  of 652 nm. At this stage, the fabricated sensor is ready to sense uric acid. The incorporation of uric acid into the reaction mixture results in a reduction of the TMB coupled with an optical change visible to the naked eye. Since oxidation and reduction take place side by side, as TMB is reduced, the uric acid is oxidized to allantoin. The mechanistic pathway of the proposed mechanism is shown in Scheme 2.

### 3.6 Optimization studies

In order to report on the fabricated sensor in its fine-tuned form, comprehensive optimization experiments were carried out as follows.

**3.6.1 Optimization of CA-Cu@BC nanozyme.** The amount of nanozyme was optimized as shown in Fig. 5(i). Different amounts of the mimic enzyme in the range of 1–7 mg were used in the experiments. The best optical transformation was achieved at 2 mg of the CA-Cu@BC nanozyme. At this amount of the mimic enzyme, the addition of uric acid results in the complete discoloration of the reaction mixture. However, a further increase in the amount of the mimic enzyme results in the overwhelming scavenging effect of the analyte. This overwhelming of the mimic enzyme results in the presence of oxidized TMB, which is reflected by the presence of a blue-green color in the reaction mixture. An increase in the amount of the mimic enzyme results in an intense blue-green color with a corresponding increase in absorbance, as shown in the figure. Hence, 2 mg of the mimic enzyme was selected as an optimal amount and used for further experiments.

**3.6.2 Optimization of pH.** pH is an important factor in reporting on the performance of a fabricated sensor. In the current work, the proposed sensor's performance was assessed in the pH range of 3–10, as shown in Fig. 5(ii). The best optical

transformation was achieved at pH 6. This behavior of the fabricated sensor could be explained by the fact that at lower pH, the TMB gets protonated. This protonation of TMB makes it resistant to oxidation due to the unavailability of electrons on the amino group. However, when the pH increases from 3 to 6, the concentration of protons decreases. At pH levels above 6, the concentration of hydroxyl ions increases in the environment of the reaction mixture. These hydroxyl ions are more likely to be attacked by the uric acid compared to the oxidized TMB. Hence, at pH levels above 6, the color remains blue-green even after the uric acid is incorporated into the reaction mixture.

**3.6.3 Effect of time.** Time is an important parameter while assessing the performance of any fabricated sensor. Sensor systems that can respond in a short period of time are highly desirable. In the current work, the sensing performance of the proposed sensor was tested in the time range of 25 to 175 seconds, as can be seen in Fig. 5(iii). It is evident from the figure that the best optical change was observed at 150 seconds. A further increase in time does not cause any change in the reaction. Pan *et al.* reported 15 minutes to be the optimal time in their work for the detection of the same analyte.<sup>33</sup>

**3.6.4 TMB concentration.** The concentration of the chromogenic substrate TMB was optimized in the molarity range of 0.3–2.1 mM, as shown in Fig. 5(iv). It is clear from the figure that the best optical response was obtained at 0.9 mM of TMB. Hence, for the onward experiments, 0.9 mM of TMB was used.

**3.6.5 Optimization of H<sub>2</sub>O<sub>2</sub>.** Hydrogen peroxide plays an important role in the fabrication of the proposed sensor. Various molarity solutions of hydrogen peroxide in the range of 0.3–2.1 mM were used to assess the performance of the fabricated sensor, as shown in Fig. 5(v). The best optical response was achieved at 1.5 mM of hydrogen peroxide. Hence, the optimal molarity of 1.5 mM of hydrogen peroxide was used for onward reactions.

### 3.7 Determination of the analytical merit of the fabricated sensing platform

Capitalizing on the successful synthesis, characterization, and optimization of the fabricated sensor, its quantitative performance was tested. For this purpose, various concentration solutions of the analyte were tested with the fabricated sensor. The fabricated platform could detect the analyte under study at a wide range of concentrations. However, the linear response of the developed sensor could be achieved in the range of 1–90  $\mu\text{M}$ , as shown in Fig. 6(i) and (ii). The linear regression coefficient in this linear range was calculated to be 0.997, indicating the higher linearity and precision of the fabricated sensor. Other key analytical indicators for the proposed sensor, such as limits of detection and quantification, were calculated to be 0.17  $\mu\text{M}$  and 0.58  $\mu\text{M}$ , respectively. The analytical performance of the fabricated sensor was compared with several other reported sensing platforms, as shown in Table 1. The results indicate that the fabricated sensor has a broad linear range and an excellent limit of detection and quantification.



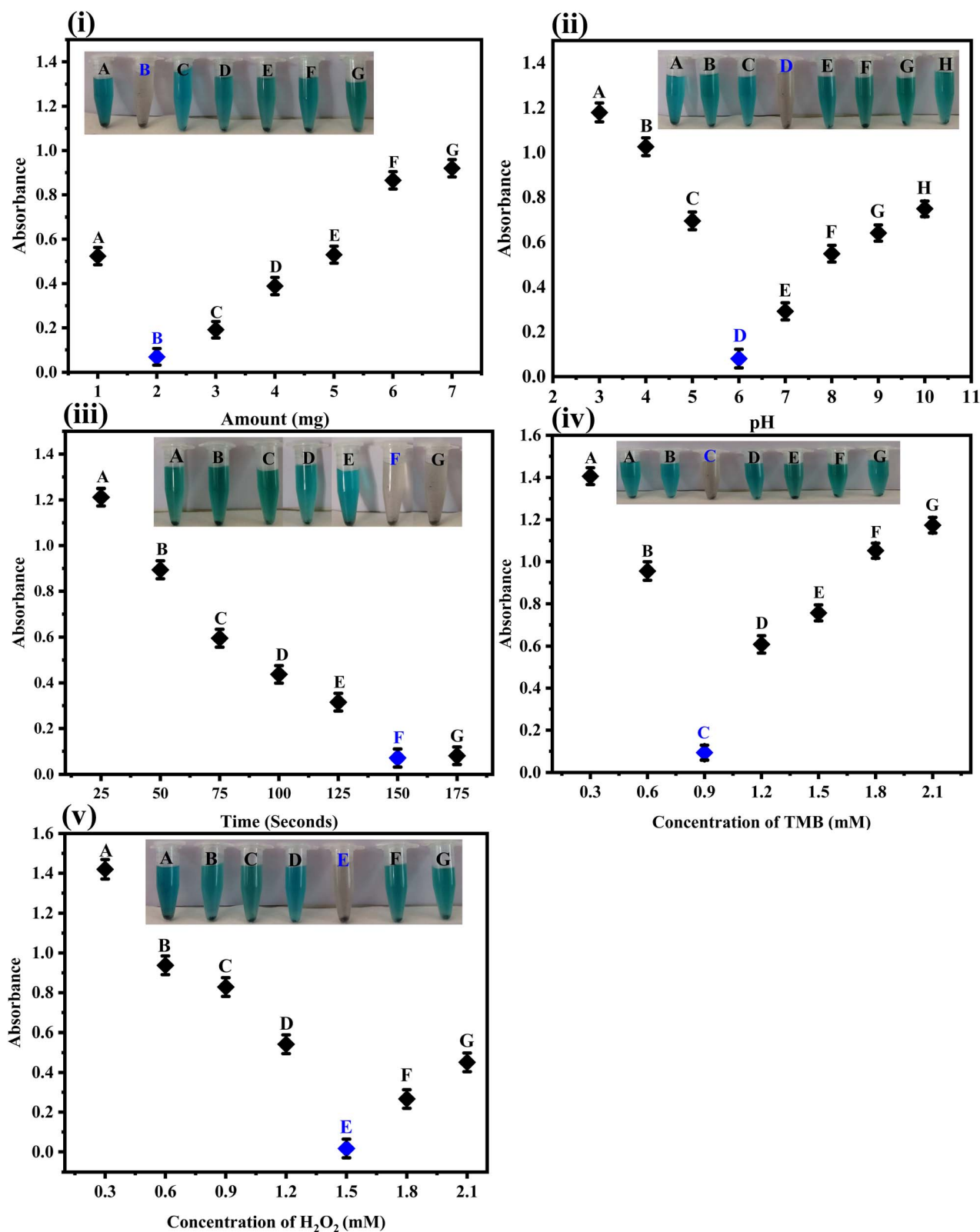


Fig. 5 (i) Shows the optimization of the amount of nanozyme in the range of 1–7 mg, with the optimal response achieved at 2 mg of the CA–Cu@BC. (ii) The proposed sensor performance was assessed in the pH range of 3–10, with the best optical transformation achieved at pH 6. (iii) The graph represents the time optimization of the proposed sensor in the range of 25–175 seconds. The optimal response in terms of color change and spectrophotometric estimation was achieved at 150 seconds. (iv) The graph shows the optimization of TMB concentration in the range of 0.3–2.1 mM, with the best response achieved at 0.9 mM of the chromogenic substrate. (v) The graph depicts the optimization of H<sub>2</sub>O<sub>2</sub> concentration in the range 0.3–2.1 mM, with the best response obtained at 1.5 mM of hydrogen peroxide.



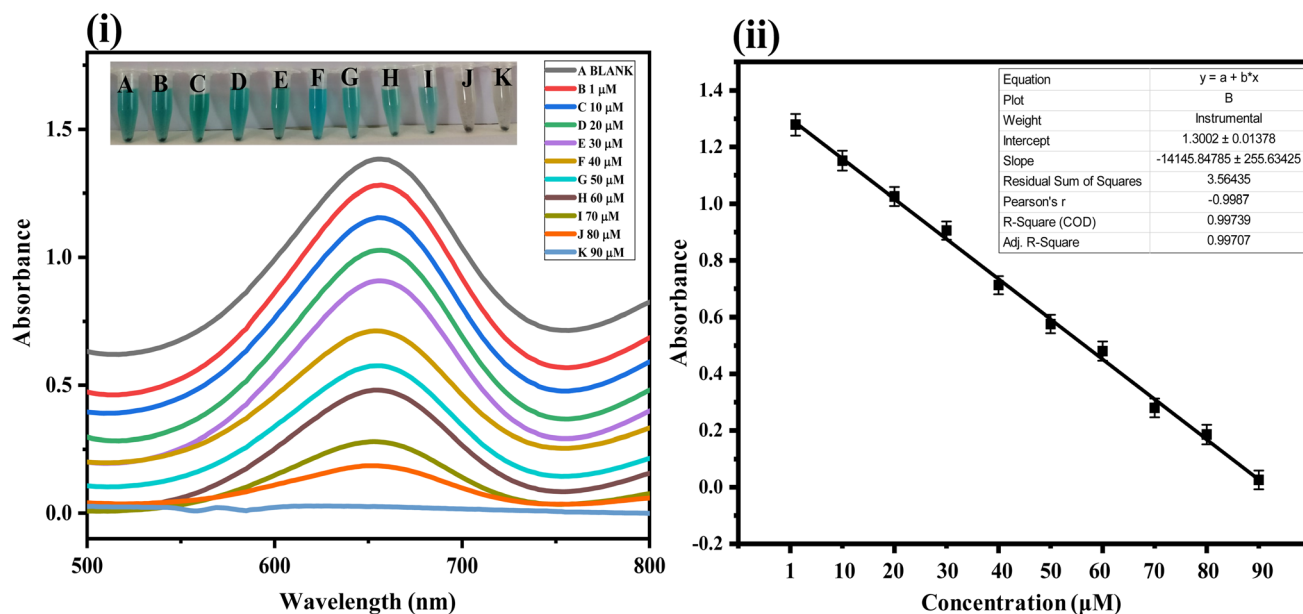


Fig. 6 The figure shows the analytical performance of the fabricated sensor. (i) Various uric acid concentration solutions in the range of 1–90  $\mu\text{M}$  were tested with the fabricated sensor. (ii) A quantitative relationship was established between the absorbance and uric acid concentration in the given range.

Table 1 Comparative analysis of the proposed sensing platform with previously reported studies

S. no	Analytical method	Linear range ( $\mu\text{M}$ )	LOD ( $\mu\text{M}$ )	References
1	HRP-CdS QDs	125–1000	125	34
2	MIL-53 (Fe)	10–40	8.9	35
3	$\text{Cu}^{2+}$ NPs	1–100	1.3	36
4	AuNP/cMWCNT/Au	10–800	10	37
5	GCE/Lys/Au-NPs	2–40	2.7	38
6	CdTeNPs	220–6000	100	39
7	MIL-53 (Fe)	10–40	8.9	40
8	Luminol- $\text{K}_3[\text{Fe}(\text{CN})_6]$	4.8–179	3	41
9	Uricase/BSA-stabilized Au nanoclusters	2.0–200	0.36	42
10	Nanocrystalline cobalt selenide TMB	2.0–40	0.5	43
11	CA-Cu@BC nanocomposite	1–90	0.17	Present work

### 3.8 Selectivity of the proposed method

Despite all the other merits of any fabricated sensor, selectivity towards the analyte of interest is a key factor in assessing the performance of a sensor. In this regard, the selectivity of the sensor was examined for a variety of potential interfering species against uric acid. These include zinc, magnesium, calcium ions, glucose, dopamine, ascorbic acid, and their mixture, as shown in Fig. 7.

### 3.9 Application of the fabricated sensor

To study the applicability of the fabricated sensor, uric acid was detected in real urine samples. For the quantitative investigation, urine samples were strategically diluted and processed for sensing through the optimized proposed sensor. Through this method, UA with varying amounts of 8, 23, and 42  $\mu\text{M}$  were

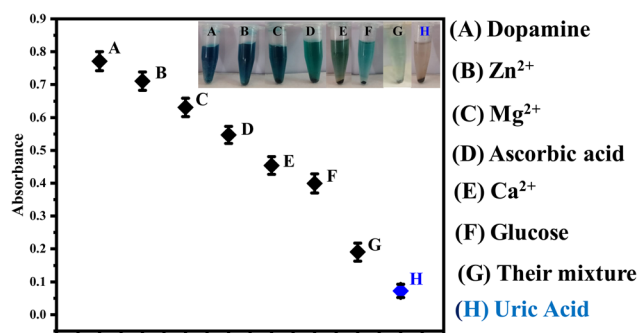


Fig. 7 Interfering studies of the proposed sensor show that it is selective for uric acid in the presence of a number of various potential interfering species.

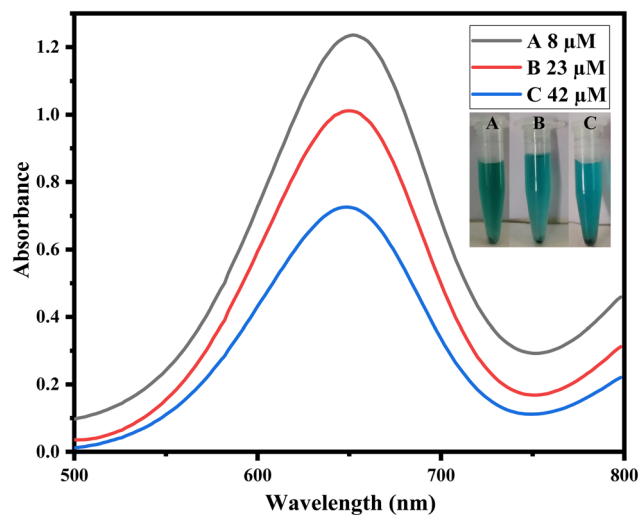


Fig. 8 Real sample analysis in urine samples with varying concentrations of uric acids such as (A) 8, (B) 23, and (C) 42  $\mu\text{M}$ .

Table 2 Application of the method to real urine samples

S. no	Initial absorbance	Final absorbance	Uric acid found ( $\mu\text{M}$ )
1	1.37	1.23 $\pm$ 0.09	0.14 $\pm$ 0.01
2	1.37	1.07 $\pm$ 0.06	0.3 $\pm$ 0.02
3	1.37	0.73 $\pm$ 0.02	0.64 $\pm$ 0.001

obtained through the already established calibration curve. Using a UV-vis spectrophotometer, the colorimetric change was confirmed, and the absorption peaks were noted at the  $\lambda_{\text{max}}$  of 652 nm. The findings indicate that the developed sensing system is capable of figuring out the amounts of uric acid in real urine samples. The change in absorption spectra of TMB corresponds well with the change in concentration of the analyte under study, as illustrated in Fig. 8. In addition, the results of the application of the method to urine samples have also been given in Table 2.

## 4 Conclusion

In conclusion, we have successfully synthesized copper biochar (Cu@BC) and capped it with citric acid to achieve citric acid-capped copper biochar (CA-Cu@BC). The entire set of necessary characterization techniques confirmed the desired synthesis. Based on the fabricated mimic enzyme, a new, easy-to-use, sensitive, low-cost, and selective optical sensor for uric acid was fabricated. Various optimization parameters were fine-tuned in order to report the newly synthesized sensor in its optimized form. Under the optimized conditions, the proposed sensing platform was able to detect uric acid in a wide linear range, with lower limits of detection and quantification when compared with the already reported sensors. The selectivity performance of the synthesized nanozyme was excellent when compared with other potential interfering species under the reported optimized conditions. The sensor system was

successfully applied to detect uric acid in real urine samples. The proposed sensor has the potential to be translated into a robust, easy-to-use, low-cost, sensitive, and selective platform for the diagnosis, management, and monitoring of uric acid-related diseases.

## Data availability

The manuscript contains the majority of the data generated in the current work. Any additional information that may be required can be requested from the corresponding author on a reasonable basis.

## Conflicts of interest

The authors declare that they have no known competing financial interests or personal relationships that could have appeared to influence the work reported in this paper. The authors declare the following financial interests/personal relationships which may be considered as potential competing interests.

## Acknowledgements

Authors wish to thank Researchers Supporting Project Number (RSP2024R171) at King Saud University Riyadh Saudi Arabia for financial support. The work is also supported by Open Foundation of Hainan International Joint Research Center of Marine Advanced Photoelectric Functional Materials (2024MAPFM01).

## References

- 1 D. Huang, Y. Cheng, H. Xu, H. Zhang, L. Sheng, H. Xu, *et al.*, The determination of uric acid in human body fluid samples using glassy carbon electrode activated by a simple electrochemical method, *J. Solid State Electrochem.*, 2015, **19**, 435–443.
- 2 Y. Li, X. Zhai, X. Liu, X. Ji and L. Wang, Voltammetric determination of uric acid in the presence of ascorbic acid and dopamine using chitosan/ionic liquid composite electrode, *Ionics*, 2014, **20**, 1247–1254.
- 3 P. Xu, R. Li, Y. Tu and J. Yan, A gold nanocluster-based sensor for sensitive uric acid detection, *Talanta*, 2015, **144**, 704–709.
- 4 U. Nishan, W. Ullah, N. Muhammad, M. Asad, S. Afridi, M. Khan, *et al.*, Development of a nonenzymatic colorimetric sensor for the detection of uric acid based on ionic liquid-mediated nickel nanostructures, *ACS Omega*, 2022, **7**, 26983–26991.
- 5 Q.-Q. Zhuang, Z.-H. Lin, Y.-C. Jiang, H.-H. Deng, S.-B. He, L.-T. Su, *et al.*, Peroxidase-like activity of nanocrystalline cobalt selenide and its application for uric acid detection, *Int. J. Nanomed.*, 2017, 3295–3302.
- 6 Y. Zhou, B. Liu, R. Yang and J. Liu, Filling in the gaps between nanozymes and enzymes: challenges and opportunities, *Bioconjugate Chem.*, 2017, **28**, 2903–2909.

- 7 P. Zhao, N. Li and D. Astruc, State of the art in gold nanoparticle synthesis, *Coord. Chem. Rev.*, 2013, **257**, 638–665.
- 8 K. Esumi, N. Takei and T. Yoshimura, Antioxidant-potentiality of gold–chitosan nanocomposites, *Colloids Surf., B*, 2003, **32**, 117–123.
- 9 D. Wei, W. Qian, Y. Shi, S. Ding and Y. Xia, Mass synthesis of single-crystal gold nanosheets based on chitosan, *Carbohydr. Res.*, 2007, **342**, 2494–2499.
- 10 A. Murugadoss and H. Sakurai, Chitosan-stabilized gold, gold–palladium, and gold–platinum nanoclusters as efficient catalysts for aerobic oxidation of alcohols, *J. Mol. Catal. A: Chem.*, 2011, **341**, 1–6.
- 11 M. Asad, N. Muhammad, N. Khan, M. Shah, M. Khan, M. Khan, *et al.*, Colorimetric acetone sensor based on ionic liquid functionalized drug-mediated silver nanostructures, *J. Pharm. Biomed. Anal.*, 2022, **221**, 115043.
- 12 U. Nishan, I. Ullah, N. Muhammad, S. Afridi, M. Asad, S. U. Haq, *et al.*, Investigation of silver-doped iron oxide nanostructures functionalized with ionic liquid for colorimetric sensing of hydrogen peroxide, *Arabian J. Sci. Eng.*, 2023, **48**, 7703–7712.
- 13 P. Parthasarathy and S. Vivekanandan, A comprehensive review on thin film-based nano-biosensor for uric acid determination: arthritis diagnosis, *World Rev. Sci. Technol. Sustain. Dev.*, 2018, **14**, 52–71.
- 14 K. Ragavan, S. R. Ahmed, X. Weng and S. Neethirajan, Chitosan as a peroxidase mimic: Paper based sensor for the detection of hydrogen peroxide, *Sens. Actuators, B*, 2018, **272**, 8–13.
- 15 U. Nishan, A. Ahmed, N. Muhammad, M. Shah, M. Asad, N. Khan, *et al.*, Uric acid quantification *via* colorimetric detection utilizing silver oxide-modified activated carbon nanoparticles functionalized with ionic liquid, *RSC Adv.*, 2024, **14**, 7022–7030.
- 16 U. Nishan, A. Niaz, N. Muhammad, M. Asad, N. Khan, M. Khan, *et al.*, Non-enzymatic colorimetric biosensor for hydrogen peroxide using lignin-based silver nanoparticles tuned with ionic liquid as a peroxidase mimic, *Arabian J. Chem.*, 2021, **14**, 103164.
- 17 U. Nishan, K. Ullah, N. Muhammad, A. Badshah, S. Afridi, N. Khan, *et al.*, Environment-Friendly and Efficient Colorimetric Sensing of Hydrogen Peroxide Based on Dalbergia sissoo Sawdust-Deposited Nickel Nanoparticles, *Waste Biomass Valorization*, 2024, 1–12.
- 18 A. Khaliq, R. Nazir, M. Khan, A. Rahim, M. Asad, M. Shah, *et al.*, Co-doped CeO<sub>2</sub>/activated C nanocomposite functionalized with ionic liquid for colorimetric biosensing of H<sub>2</sub>O<sub>2</sub> *via* peroxidase mimicking, *Molecules*, 2023, **28**, 3325.
- 19 U. Nishan, T. Zahra, A. Badshah, N. Muhammad, S. Afridi, M. Shah, *et al.*, Colorimetric sensing of hydrogen peroxide using capped *Morus nigra*-sawdust deposited zinc oxide nanoparticles *via* *Trigonella foenum* extract, *Front. Bioeng. Biotechnol.*, 2024, **12**, 1338920.
- 20 J. Wang, X. Fang, Y. Zhang, X. Cui, H. Zhao, X. Li, *et al.*, A simple and rapid colorimetric probe for uric acid detection based on redox reaction of 3, 3', 5, 5'-tetramethylbenzidine with HAuCl<sub>4</sub>, *Colloids Surf., A*, 2018, **555**, 565–571.
- 21 M. Ahmad, A. U. Rajapaksha, J. E. Lim, M. Zhang, N. Bolan, D. Mohan, *et al.*, Biochar as a sorbent for contaminant management in soil and water: a review, *Chemosphere*, 2014, **99**, 19–33.
- 22 R. Amen, H. Bashir, I. Bibi, S. M. Shaheen, N. K. Niazi, M. Shahid, *et al.*, A critical review on arsenic removal from water using biochar-based sorbents: the significance of modification and redox reactions, *Chem. Eng. J.*, 2020, **396**, 125195.
- 23 E. Wen, X. Yang, H. Chen, S. M. Shaheen, B. Sarkar, S. Xu, *et al.*, Iron-modified biochar and water management regime-induced changes in plant growth, enzyme activities, and phytoavailability of arsenic, cadmium and lead in a paddy soil, *J. Hazard. Mater.*, 2021, **407**, 124344.
- 24 A. Banu, A. M. Antony, B. S. Sasidhar, S. A. Patil and S. A. Patil, Palladium Nanoparticles Grafted onto Phytochemical Functionalized Biochar: A Sustainable Nanozyme for Colorimetric Sensing of Glucose and Glutathione, *Molecules*, 2023, **28**, 6676.
- 25 V. Mikelashvili, S. Kekutia, J. Markhulia, L. Saneblidze, N. Maisuradze, M. Kriechbaum, *et al.*, Synthesis and characterization of citric acid-modified iron oxide nanoparticles prepared with electrohydraulic discharge treatment, *Materials*, 2023, **16**, 746.
- 26 M. Solioz and M. Solioz, “Copper—A Modern Bioelement”, *Copper and Bacteria: Evolution, Homeostasis and Toxicity*, 2018, pp. 1–9.
- 27 S. H. Baek, J. Roh, C. Y. Park, M. W. Kim, R. Shi, S. K. Kailasa, *et al.*, Cu-nanoflower decorated gold nanoparticles-graphene oxide nanofiber as electrochemical biosensor for glucose detection, *Mater. Sci. Eng., C*, 2020, **107**, 110273.
- 28 N. S. Shah, J. A. Khan, M. Sayed, J. Iqbal, Z. U. H. Khan, N. Muhammad, *et al.*, Nano-zerovalent copper as a Fenton-like catalyst for the degradation of ciprofloxacin in aqueous solution, *J. Water Process Eng.*, 2020, **37**, 101325.
- 29 J. Iqbal, N. S. Shah, M. Sayed, N. K. Niazi, M. Imran, J. A. Khan, *et al.*, Nano-zerovalent manganese/biochar composite for the adsorptive and oxidative removal of Congo-red dye from aqueous solutions, *J. Hazard. Mater.*, 2021, **403**, 123854.
- 30 N. H. Lam, R. P. Smith, N. Le, C. T. T. Thuy, M. S. Tamboli, A. M. Tamboli, *et al.*, Evaluation of the structural deviation of Cu/Cu<sub>2</sub>O nanocomposite using the X-ray diffraction analysis methods, *Crystals*, 2022, **12**, 566.
- 31 D. S. Kozak, R. A. Sergiienko, E. Shibata, A. Iizuka and T. Nakamura, Non-electrolytic synthesis of copper oxide/carbon nanocomposite by surface plasma in super-dehydrated ethanol, *Sci. Rep.*, 2016, **6**, 21178.
- 32 L. Xu, J. Li, H. Sun, X. Guo, J. Xu, H. Zhang, *et al.*, In situ growth of Cu<sub>2</sub>O/CuO nanosheets on Cu coating carbon cloths as a binder-free electrode for asymmetric supercapacitors, *Front. Chem.*, 2019, **7**, 420.
- 33 Y. Pan, Y. Yang, Y. Pang, Y. Shi, Y. Long and H. Zheng, Enhancing the peroxidase-like activity of ficin *via* heme

- binding and colorimetric detection for uric acid, *Talanta*, 2018, **185**, 433–438.
- 34 N. E. Azmi, N. I. Ramli, J. Abdullah, M. A. A. Hamid, H. Sidek, S. Abd Rahman, *et al.*, A simple and sensitive fluorescence based biosensor for the determination of uric acid using H<sub>2</sub>O<sub>2</sub>-sensitive quantum dots/dual enzymes, *Biosens. Bioelectron.*, 2015, **67**, 129–133.
- 35 J. Lu, Y. Xiong, C. Liao and F. Ye, Colorimetric detection of uric acid in human urine and serum based on peroxidase mimetic activity of MIL-53 (Fe), *Anal. Methods*, 2015, **7**, 9894–9899.
- 36 H.-F. Lu, J.-Y. Li, M.-M. Zhang, D. Wu and Q.-L. Zhang, A highly selective and sensitive colorimetric uric acid biosensor based on Cu (II)-catalyzed oxidation of 3, 3', 5, 5'-tetramethylbenzidine, *Sens. Actuators, B*, 2017, **244**, 77–83.
- 37 N. Chauhan and C. S. Pundir, An amperometric uric acid biosensor based on multiwalled carbon nanotube–gold nanoparticle composite, *Anal. Biochem.*, 2011, **413**, 97–103.
- 38 T. L. Le, Q. K. Dinh, T. H. Tran, H. P. Nguyen, T. L. H. Hoang and Q. H. Nguyen, Synthesis of water soluble chitosan stabilized gold nanoparticles and determination of uric acid, *Adv. Nat. Sci.: Nanosci. Nanotechnol.*, 2014, **5**, 025014.
- 39 D. Jin, M.-H. Seo, B. T. Huy, Q.-T. Pham, M. L. Conte, D. Thangadurai, *et al.*, Quantitative determination of uric acid using CdTe nanoparticles as fluorescence probes, *Biosens. Bioelectron.*, 2016, **77**, 359–365.
- 40 M. N. Cardoza-Contreras, J. M. Romo-Herrera, L. A. Ríos, R. García-Gutiérrez, T. Zepeda and O. E. Contreras, Single ZnO nanowire-based gas sensors to detect low concentrations of hydrogen, *Sensors*, 2015, **15**, 30539–30544.
- 41 D. He, Z. Zhang, Y. Huang, Y. Hu, H. Zhou and D. Chen, Chemiluminescence microflow injection analysis system on a chip for the determination of uric acid without enzyme, *Luminescence*, 2005, **20**, 271–275.
- 42 H. Zhao, Z. Wang, X. Jiao, L. Zhang and Y. Lv, Uricase-based highly sensitive and selective spectrophotometric determination of uric acid using BSA-stabilized Au nanoclusters as artificial enzyme, *Spectrosc. Lett.*, 2012, **45**, 511–519.
- 43 Q.-Q. Zhuang, Z.-H. Lin, Y.-C. Jiang, H.-H. Deng, S.-B. He, L.-T. Su, *et al.*, Peroxidase-like activity of nanocrystalline cobalt selenide and its application for uric acid detection, *Int. J. Nanomed.*, 2017, **12**, 3295.